Nanoarchitectonics of Hydrogel-derived Ultrahigh Surface Area Nanoporous Carbon Materials with Enhanced Supercapacitance Performance

Nadiia Velychkivska,[1,2,*] Anna Golunova,[2] Viktoria Oleksa,[1,2] Jiří Brus,[2] Pragati A. Shinde,[1] Abin Sebastian,[1] Renzhi Ma,[1] Katsuhiko Ariga,[1,3] Yusuke Yamauchi,[4,5,6] Jonathan P. Hill,[1,*] Jan Labuta,[1,*] and Lok Kumar Shrestha[1,7,*]

[1]Research Center for Materials Nanoarchitectonics (MANA), National Institute for Materials Science (NIMS), 1-1 Namiki, Tsukuba, Ibaraki 305-0044, Japan
[2]Institute of Macromolecular Chemistry, AS CR, Heyrovsky Sq. 2, 162 06 Prague 6, Czech Republic
[3]Department of Advanced Materials Science, Graduate School of Frontier Sciences, The University of Tokyo, 5-1-5 Kashiwanoha, Kashiwa 277-8561, Chiba, Japan
[4]Australian Institute for Bioengineering and Nanotechnology, The University of Queensland, Brisbane, Queensland 4072, Australia
[5]Department of Materials Process Engineering, Graduate School of Engineering, Nagoya University, Nagoya, Aichi 464-8603, Japan
[6]Department of Chemical and Biomolecular Engineering, Yonsei University, 50 Yonsei-ro, Seodaemun-gu, Seoul 03722, South Korea
[7]Department of Materials Science, Institute of Pure and Applied Sciences, University of Tsukuba 1-1-1, Tennodai, Tsukuba 305-8573, Ibaraki, Japan
Corresponding author: Research Center for Materials Nanoarchitectonics (MANA), National Institute for Materials Science (NIMS), 1-1 Namiki, Tsukuba, Ibaraki 305-0044, Japan. Email:SHRESTHA.Lokkumar@nims.go.jp

Lok Kumar Shrestha
Lok Kumar Shrestha received a Ph.D. Degree from Yokohama National University in 2008. He joined the National Institute for Materials Science (NIMS) as an ICYS-MANA researcher in 2010. Currently he is a Principal Researcher at the Research Centre for Materials Nanoarchitectonics (MANA), NIMS. He has also been appointed as Associate Professor at the University of Tsukuba.

Abstract
In the era of the decarbonization economy, supercapacitors offer a realistic solution to the energy storage problem due to their rapidly chargeable electrical double layers. Here we present the energy performance of ultrahigh surface area nanoporous carbon materials having abundant hierarchical micro/mesopores obtained by *in situ* potassium carbonate (K_2CO_3) activation of polyacrylamide (PAM) hydrogel. The resulting nanoporous carbon materials obtained by the carbonization of the hydrogel in the temperature range 600 to 900 °C possess high BET surface areas up to ca. 3038 m^2 g^{-1} for the material prepared at 800 °C (PAM_4-K800). Electron microscopy analyses revealed the formation of micro/mesoporous amorphous carbon structures. Surface composition and nitrogen and oxygen doping of the carbon matrix were verified by X-ray photoelectron spectroscopy (XPS). The electrochemical supercapacitance performance was tested using a three-electrode system in an aqueous electrolyte (1M H_2SO_4). The optimal sample (PAM_4-K800) achieved the largest value of specific capacitance of 313.3 F g^{-1} at a current density of 1 A g^{-1}, with excellent capacitance retention of 97.5% after 10,000 charge/discharge cycles. Furthermore, a symmetric supercapacitor device prepared using the optimum material delivered a high energy density of 12.3 Wh kg^{-1} at a high power density of 309.4 W kg^{-1} and an outstanding cycle life of 95.9% after 10,000 cycles. The outstanding electrochemical performance of PAM hydrogel-derived carbon materials makes them promising candidates for high-performance supercapacitor applications.

Keywords: Polyacrylamide (PAM) hydrogel, hierarchically porous carbon, supercapacitor

Graphical abstract

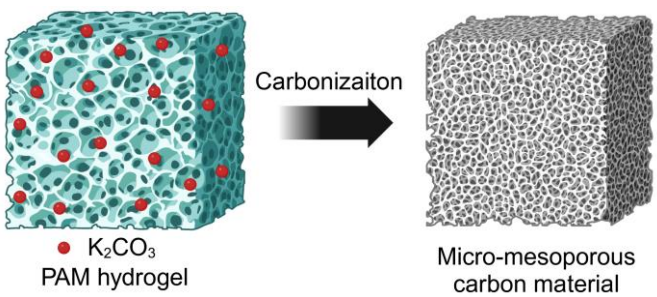

1. Introduction

In the era of a climate-neutral society, sustainable development pathways are in high demand to deliver advanced large-scale energy storage and energy conversion solutions.[1] In this regard, supercapacitors can provide an opportunity for enhancement of storage

capacities due to their superior power density, rapid charging, stable/long cycle life performances, and almost instantaneous release of large quantities of energy .[2–4] Supercapacitors store charge by physical ion adsorption/desorption processes at the electrode/electrolyte interface (in the case of electrochemical double-layer capacitors (EDLCs)), and through non-diffusion limited, fast faradaic redox reactions (in the case of pseudocapacitive materials).[5–7] Supercapacitors are used extensively for storage purposes in renewable applications such as solar and wind energy generation, in electric vehicles, and for management of building energy consumption.[8–10] To meet the rising requirement for effective energy storage supercapacitors, the selection and design of materials used as electrodes in these devices is critical. Carbonaceous materials are commonly chosen as supercapacitor electrode materials due to their excellent cost-effectiveness, high surface areas with hierarchically evolved micro/meso porosity, high thermal stabilities and electrical conductivity, stable charge-discharge cycling performances, and excellent cyclic durabilities. They include activated carbons,[11–14] from both natural and synthetic sources, carbon aerogels and graphene,[15–18] carbon foams,[19,20] carbide-derived carbons,[21,22] and carbon nanotubes.[23,24] The specific capacitance (C_s) value, together with energy and power densities, strongly depends on the surface area, pore-size distribution, and pore availability for the electrolyte ions. Consequently, to enhance the capacitive performance of the supercapacitor, materials having high surface areas with suitable pore size distributions, which would allow fast mass and ion transport through the porous network, are required.

There are several methods to modify the texture and surface of carbon materials using chemical, physical, or hydrothermal carbonization methods.[25] Chemical activation, in contrast to the other methods, leads to the formation of carbon materials with high or ultrahigh surface areas and hierarchically layered porous structures. In this process, chemical activators including alkaline or alkali metal hydroxides and salts KOH, K_2CO_3, NaOH, $ZnCl_2$, $KHCO_3$, and mixtures of salts $ZnCl_2$-KCl, K_2CO_3-Na_2CO_3, LiCl-KCl are commonly used.[25–29] K_2CO_3 is an attractive chemical activator due to its low cost, low toxicity, and environmental friendliness.[30–32] In this case, a complex carbon architecture is formed by the following mechanism. When potassium carbonate reacts with the carbon precursor under an inert atmosphere, the following reactions occur (Equations 1-3):

$$K_2CO_3 + 2C \rightarrow 2K + 3CO\uparrow \quad (1)$$

$$K_2CO_3 \rightarrow K_2O + CO_2\uparrow \quad (2)$$

$$K_2O + C \rightarrow 2K + CO\uparrow \quad (3)$$

After reduction of potassium carbonate. metallic potassium intercalates and expands the carbon network while gaseous carbon monoxide exfoliates the carbon sheets, creating a porous carbon architecture (Equation 1). Potassium oxide is obtained as an intermediate (Equation 2), which is later also reduced to potassium and carbon monoxide (Equation 3). The residual potassium byproducts in the carbon structures are then eliminated by thorough washing using water, which further enhances the porosity.

Porous carbonaceous electrode materials for supercapacitors can also be prepared using natural carbon sources, such as biomass, wood, and coal.[33–35] For instance, Zhao et al. prepared rodlike KOH-activated - carbon material derived from tobacco, which exhibited a specific capacitance of 286.6 F g^{-1} at current density 0.5 A g^{-1} measured in 6M KOH electrolyte in a three-electrode setup.[36] In other work, an acacia wood-based electrode activated with KOH exhibitrd a specific capacitance of 224.92 F g^{-1} at 0.5 A g^{-1} measured in 2M KOH in a three-electrode system.[37] However, the composition of carbon materials from different natural sources varies depending on the origin of the material, making it difficult to reproduce specific capacitances of the resulting electrodes.

In order to overcome this obstacle, synthetic carbon materials can be used since they offer a high degree of control over morphological properties, are easy to prepare, and can be cost-effective. In this respect, hydrogel-derived carbon materials appear to be especially suitable candidates for energy storage applications due to their tunable textural parameters.[38] Of the available materials, polyacrylamide (PAM) hydrogels are particularly interesting due to their chemical structure consisting of (-CH_2-CH-CO-NH_2-) units, which presents a source of self-doping by oxygen and nitrogen functionalities in the 3D network.[39–44] For example, the hierarchically porous carbon electrode prepared from the KOH-activated resorcinol/formaldehyde-polyacrylamide interpenetrating polymer network showed a high specific surface area of 2544 m^2 g^{-1} and specific capacitance of 261 F g^{-1} at 1.0 A g^{-1} measured in 6M KOH.[45] Moreover, Gao et al. obtained carbon materials from $ZnCl_2$-activated PAM hydrogel (Free-PC) and polypyrrole-PAM (PPC) hydrogels with surface areas of 1363 m^2 g^{-1} and 1797 m^2 g^{-1}, respectively. In a three-electrode system, these self-oxygen/nitrogen-doped carbon materials exhibited high specific capacitance values of 262 F g^{-1} and 398 F g^{-1} at a current density of 0.5 A g^{-1} for Free-PC and PPC, respectively.[46] The presence of N,O dopants contributes favorably to the electrode surface wettability and induces pseudocapacitance that leads to high specific capacitance. Similarly, carbon materials prepared from MgAl-layered double hydroxides and polyacrylamide showed promising electrochemical performance values (356 F g^{-1} at 0.5 A g^{-1}) and a good durabilities.[47] Since PAM-hydrogel carbons are still emerging electrode materials for supercapacitor applications, there remains a gap in the knowledge of their textural and electrochemical properties.

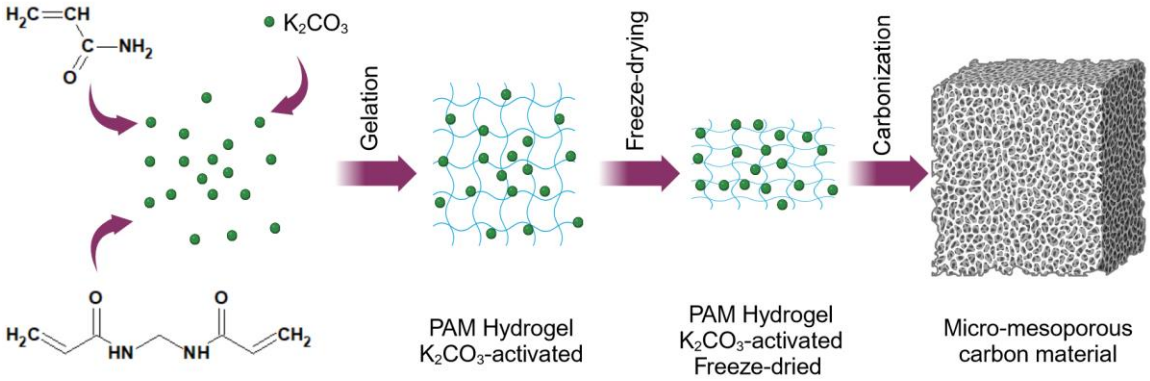

Scheme 1. Schematic representation of the synthetic route for PAM hydrogel-derived carbon materials

In this work, we present the preparation, characterization, and electrochemical performance of intrinsically N,O doped polyacrylamide hydrogel-derived carbon materials with ultra-high surface areas, and well-developed micro and meso pores for supercapacitor applications. The hydrogels were prepared from acrylamide and N,N-methylenebisacrylamide (MBA), then freeze-dried and annealed at high temperatures (600–900 °C). Hierarchical micro and mesoporous architectures of the carbon materials obtained were adjusted by *in situ* introduction of a chemical activating agent K_2CO_3 with a subsequent annealing process (Scheme 1). Of the carbon materials obtained, the sample annealed at 800 °C (PAM_4-K800) showed the highest BET surface area of 3038.4 $m^2\ g^{-1}$ with the largest pore volume of 1.852 $cm^3\ g^{-1}$. The presence of nitrogen and oxygen functionalities on the synthesized carbon surfaces was confirmed by XPS analysis. According to the physicochemical characterization, three-electrode electrochemical measurements revealed otstanding performances of the carbon materials as supercapacitor electrode materials. Of the materials, PAM_4-K800 demonstrated a superior specific capacitance of 313.3 F g^{-1} at a current density of 1 A g^{-1} in an aqueous 1M H_2SO_4electrolyte. The electrode material is stable even after 10000 cycles with a cycling performance of 97.5%. Based on the electrochemical data, polyacrylamide hydrogel-derived hierarchically porous carbon materials have strong potential in high-performance supercapacitor applications.

2. Experimental

2.1 Materials

Acrylamide (AM), sodium sulfite (Na_2SO_3), and potassium persulfate ($K_2S_2O_8$) were purchased from Wako Pure Chemical Industries, Tokyo, Japan. N,N′-methylenebisacrylamide (MBA) was purchased from TCI, Tokyo, Japan. Potassium carbonate (K_2CO_3) was purchased from Nacalai Tesque, Kyoto, Japan. Deionized (DI) water (H_2O) was obtained using a Direct Q 3UV water purification system, Merck Millipore, Darmstadt, Germany; Resistivity ≥ 18 MΩ cm at 25 °C). The hydrogels were prepared in DI water, and the resulting carbon materials were also washed using DI water.

2.2 Preparation of porous carbon materials from PAM hydrogels

PAM hydrogels were synthesized as described in our previous research.[48] Briefly, AM (360 mg), MBA (40 mg), and K_2CO_3 (500 mg) were loaded into a 30 mL glass vial and dissolved in DI water (8 g). Then, the mixture was degassed, and 1 mL of Na_2SO_3 (10 mg) and 1 mL of $K_2S_2O_8$ (20 mg) were injected into the deoxygenated reaction mixture to initiate the free radical (co)polymerization reaction. After gelation was complete, the hydrogels were freeze-dried, annealed at various temperatures, and thoroughly washed with DI water. The samples are referred to according to their compositions as follows: PAM_4-KX, where subscript index 4 is the concentration of PAM hydrogel (4 wt%), X is the annealing temperature (600, 700, 800, 900 °C), and K indicates the presence of the chemical activation agent (K_2CO_3).

2.3 Materials characterization

PAM hydrogel-derived carbon materials were studied by thermogravimetric analysis (TGA) using STA 2500 (Regulus, Netzsch, Wittelsbacherstraße, SELB, Germany) under an inert atmosphere of nitrogen at a heating rate of 10 °C per minute. Raman scattering spectroscopy at a neon laser excitation wavelength of 532.09 nm (NRS-3100, JASCO, Tokyo, Japan) was applied to characterize graphitic and disordered states of PAM hydrogel-derived carbons. The amorphous structure of PAM hydrogel-derived carbons was confirmed by powder X-ray diffraction (XRD) (Rigaku X-ray diffractometer, RINT, Tokyo, Japan) with the following measurement conditions: the scan range of 2θ = 15 – 50°; V = 40 kV; I = 40 mA; Cu-Kα radiation source; 25 °C. X-ray photoelectron spectroscopy (XPS) (Quantera SXM instrument, ULVAC-PHI, Chanhassen,

MN, USA) was used to study the surface composition of PAM hydrogel-derived carbon materials. Fourier-transform infrared (FTIR) spectroscopy NICOLET iS20 (Thermo-Fisher Scientific, Waltham, MA, USA) proved the presence of nitrogen and oxygen-containing functional groups in PAM hydrogel and corresponding carbon samples. Scanning electron microscopy (SEM) (S-4800, Hitachi Co., Ltd., Japan, V = 10 kV) and transmission electron microscopy (TEM) (JEM2100F instrument, JEOL, Tokyo, Japan, V = 200 kV) were used for examination of the surface morphologies of PAM hydrogel-derived carbon materials. To reduce charging effects during SEM imaging, the samples were coated with platinum (~2 nm) using a Hitachi S-2030 ion coater. Brunauer–Emmett–Teller (BET) specific surface area and porosity method was used to study the textural properties of PAM hydrogel-derived carbons. N_2 adsorption/desorption measurements were made under high vacuum at 77 K using (Quantachrome Autosorb-iQ2 instrument, Boynton Beach, FL, USA). Before the BET measurements, carbon samples were degassed under low pressure at 120 °C for 24 h. The density functional theory (DFT) and Barrett–Joyner–Halenda (BJH) methods were used to calculate the pore dimensions and pore volumes of the studied carbon samples.

2.4 Electrochemical measurements

The electrochemical performance was evaluated using galvanostatic charge–discharge (GCD), cyclic voltammetry (CV), and electrochemical impedance spectroscopy (EIS) measurements. GCD, CV, and EIS measurements were executed in a three-electrode setup in 1M H_2SO_4 electrolyte at 25 °C using an ALS CHI 660E workstation (CH Instruments, Inc. Austin, TX, USA). The working electrode was coated with the electrode material (1 cm × 1 cm) on graphite paper which had previously been etched in ethanol. Electrode material was prepared by grinding a mixture of active PAM hydrogel-derived carbon material, carbon black, and polyvinylidene fluoride (mass fraction: 80%: 10%: 10%) in N-methyl-2-pyrrolidone (NMP). The homogenous slurry was applied onto the electrode, which was then dried in air overnight at 80 °C. The mass of the active material on the prepared electrodes was 2.0-2.5 mg. A platinum wire was used as a counter-electrode, and Ag/AgCl was used as a reference electrode. EIS measurements were performed at open circuit potential conditions in the frequency range of 0.01 Hz–100 kHz at an amplitude of 5 mV. GCD data were used for the estimation of specific capacitance values (C_s, F g^{-1}) using Equation 4:

$$C_s = \frac{I \cdot t_d}{m \cdot \Delta V} \quad (4)$$

where I is the discharge current (in A), t_d is the discharge time (in s), m is the active mass of the carbon material loaded on the working electrode (in g), and ΔV is the potential window (1.1 V).

The charge storage behavior of PAM_4-K800 was precisely evaluated by the power law using the following Equation 5:

$$i = av^b \quad (5)$$

where i (A g^{-1}) is the sum of surface-controlled (capacitive) and diffusion-controlled current contributions, v is the applied scan rate (mV s^{-1}) a and b are variable parameters. If the b value is ~1, then a surface-controlled charge storage mechanism dominates. If the b value is ~0.5, then a diffusion-controlled energy storage process prevails.Surface-controlled and diffusion-controlled contributions can be obtained quantitatively from Equation 6:

$$i(V) = k_1 v + k_2 v^{1/2} \quad (6)$$

where i, v, k_1, and k_2 indicate the current, scan rate, and two constant parameters, respectively.

A symmetric supercapacitor cell was assembled with a similar mass loading of 1.2 mg using 1 M H_2SO_4 electrolyte. Galvanostatic charge–discharge tests (current density of 0.5–20 Ag^{-1}) and cyclic voltammetry measurements (scanning rate of 5–100 mV s^{-1}) were conducted using a BioLogic station VSP-3e (Grenoble, France).

The energy density and power density of the symmetric supercapacitor device were calculated using the following Equations 7 and 8

$$E = \frac{0.5 \cdot C_s(\Delta V^2)}{3.6} \quad (7)$$

$$P = \frac{3600 \cdot E}{t_d} \quad (8)$$

where E is energy density (Wh kg^{-1}) and P is power density (W kg^{-1}).

3. Results and discussion

Thermogravimetric analysis (TGA) was used to study the thermal stability of synthesized K_2CO_3-activated PAM hydrogel (Figure 1a). Below 200 °C, material weight loss occurs due to the evaporation of residual moisture from the hydrogel structure. Between 200 °C

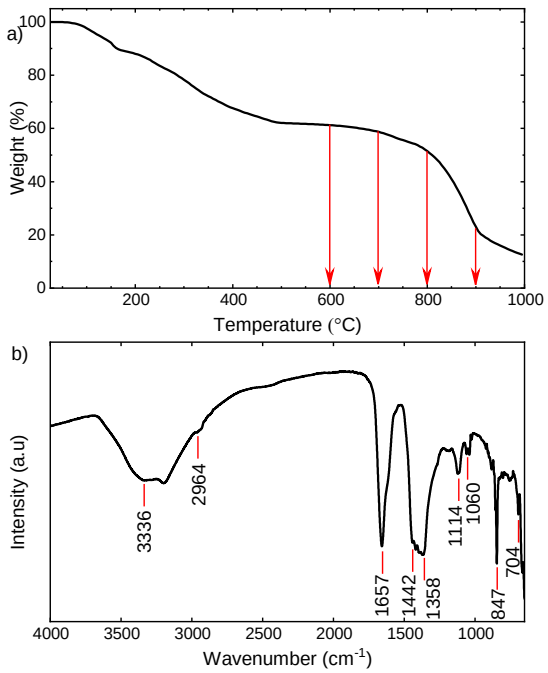

Figure 1. (a) TGA. Red arrows on the TGA graph show the carbonization temperatures used. (b) FTIR spectrum of K_2CO_3-activated PAM hydrogel.

and 500 °C, the collapse of the hydrogel network takes place, which is associated with the formation of imides and further random decomposition accompanied by the release of volatile gases, including ammonia, carbon dioxide, and water.[49] Above 500 °C, the carbon material is fully developed, so that the following carbonization temperatures were selected for further examination: 600 °C, 700 °C, 800 °C, and 900 °C. K_2CO_3-activated PAM hydrogel was further characterized by using FTIR spectroscopy (Figure 1b). The FTIR spectrum contains the following bands due to PAM at 3336 cm^{-1}, 2964 cm^{-1}, 1657 cm^{-1}, 1442 cm^{-1}, which are N-H, C-H, C=O (carbonyl), and C-N stretching vibrations, respectively.[50,51] Moreover, FTIR analysis reveals that the higher the carbonization temperature, the lower the content of oxygen-containing (band at 1657 cm^{-1}) and nitrogen-containing (band at 1442 cm^{-1}) functional groups in the carbon structure (Figure S1).

To estimate the surface area of the PAM hydrogel-derived carbon materials, N_2 adsorption/desorption experiments were carried out, the results of which are shown in Figure 2a. PAM_4-800, which is a reference sample directly carbonized at 800 °C but not activated using potassium carbonate (Figure 2a, black curve), shows a Type III isotherm with BET surface area of only 245,3 m^2 g^{-1}.[52] The presence of K_2CO_3 as an activation agent has an significant effect on the textural properties

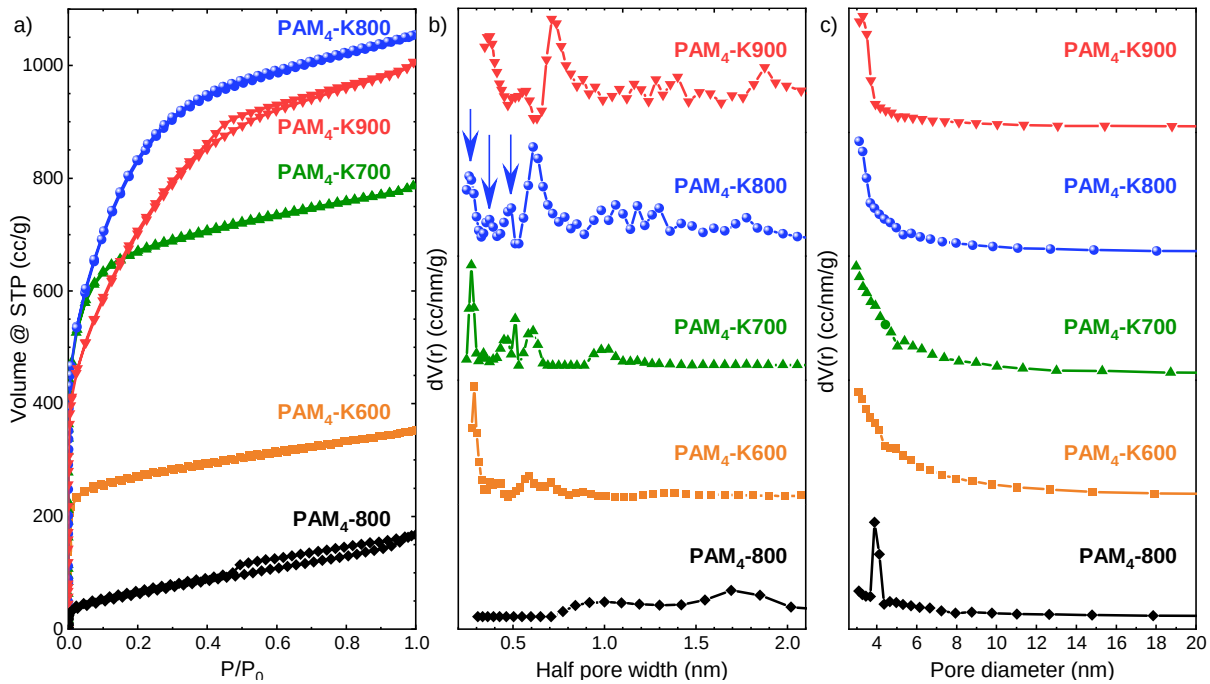

Figure 2. Textural properties obtained by nitrogen sorption measurements. (a) Nitrogen adsorption/desorption isotherms at 77 K of PAM_4-800, PAM_4-K600, PAM_4-K700, PAM_4-K800, PAM_4-K900 samples; (b) pore-size-distribution profiles from the density functional theory (DFT) method; and (c) pore-size-distribution profiles obtained from the Barrett–Joyner–Halenda (BJH) model.

Table 1. Textural properties of PAM hydrogel-derived carbon materials[1].

Sample	S_{BET} ($m^2\ g^{-1}$)	S_{micro} ($m^2\ g^{-1}$)	S_{meso} ($m^2\ g^{-1}$)	V_p ($cm^3\ g^{-1}$)	V_{micro} ($cm^3\ g^{-1}$)	V_{meso} ($cm^3\ g^{-1}$)	W_p (nm)	D_p (nm)
PAM_4-800	245.3	212.8	142.4	0.435	0.242	0.193	2.594	3.90
PAM_4-K600	1014.1	1122.9	93.3	0.640	0.501	0.139	0.287	3.10
PAM_4-K700	2526.9	2511.0	143.3	1.362	1.162	0.200	0.273	2.97
PAM_4-K800	3038.4	2669.9	209.1	1.852	1.567	0.278	0.610	3.12
PAM_4-K900	2567.8	2326.2	342.7	1.898	1.487	0.411	0.610	3.31

[1] S_{BET} = BET surface area, S_{micro} = micropore surface area, S_{meso} = mesopore surface area, V_p = total pore volume, V_{micro} = pore volume from micropores, V_{meso} = pore volume from mesopores, W_p = average half pore width, D_p = average mesopore diameter.

of the carbon materials obtained substantially increasing their surface areas. The mechanism of K_2CO_3 activation has already been discussed.[48] In the case of K_2CO_3-activated PAM hydrogel-derived carbons, a temperature increase from 600 to 800 °C leads to an increase in the formation of high surface area microporous carbons. PAM_4-K600, PAM_4-K700, and PAM_4-K800 show typical Type I isotherms with high nitrogen uptake in the low relative pressure region (P/P_0 < 0.1), which confirms the presence of a significant quantity of micropores (Figure 2a).

Carbonization at 900 °C (PAM_4-K900) stimulates coalescence of the micropores with further arrangement as mesopores. The characteristic mesoporous capillary condensation behavior is represented by mixed Type I/Type IV isotherms with a hysteresis loop in the middle of the relative pressure region (0.4< P/P_0 < 0.6). DFT (Figure 2b) and BJH (Figure 2c) models provide information about pore-size-distribution profiles of the carbon materials obtained and further confirmed their hierarchical micro/mesoporous nature. The well-developed micro/mesoporosity of carbon materials is a predominant factor in effective electrolyte diffusion onto the surface of a supercapacitor electrode.

The textural properties of PAM hierarchically interconnected micro-mesoporous carbon materials are shown in Table 1 and indicate the evident dependency of structural parameters on carbonization temperature, i.e. higher temperature induces an increase in specific surface area. However, at 900 °C, the formation of mesopores due to the coalescence of micropores commences, resulting in a decrease in microporous surface area. As a result, the optimal sample among these carbon materials is PAM_4-K800 (BET surface area: 3038.4 $m^2\ g^{-1}$, pore volume: 1.852 $cm^3\ g^{-1}$), with the highest degree of microporosity and sufficient total pore volume suggesting excellent energy storage capabilities for this material.

In order to gain insight into the inner structure of carbon materials the morphology was studied. Figure 3 shows electron micrographs (SEM: Figure 3a,b; TEM: Figure 3c,d) of the K_2CO_3-activated sample with the optimal surface textural properties, PAM_4-K800. Additional SEM images (Figure S2) and TEM images (Figure S3) are supplied in the Supplementary Information. At the macroscale, the sample morphology of the carbonized sample has a honeycomb-like irregular structure (Figure 3a). High-resolution SEM (Figure 3b and Figure S2) and TEM images (Figure 3c,d and Figure S3) show well-developed micro/mesoporous amorphous carbon structures due to K_2CO_3 activation. Directly carbonized reference sample, PAM_4-800 does not exhibit porous surface structure (Figure S4). However, K_2CO_3-activated carbon materaisl obtained at different carbonization temperatures shows similar hierarchical micro/mesopores architectures to that of the optimal sample, well-defined pore size distribution, large pore volume, and high specific surface area (Figure S5: SEM images of PAM_4-K600, Figure S6: SEM images of PAM_4-K700, Figure S7: SEM images of PAM_4-K900,

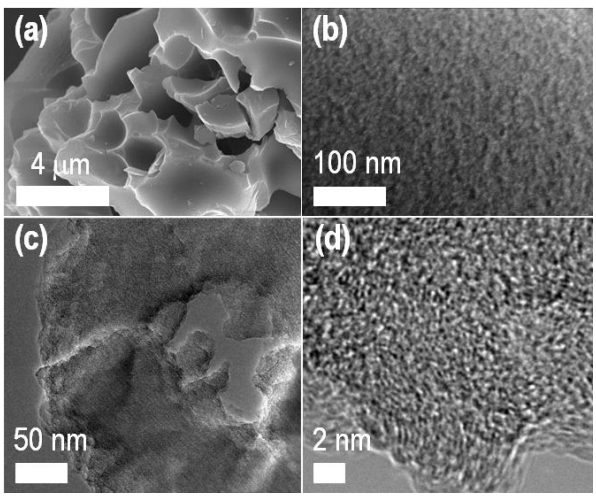

Figure 3. (a) Electron microscopy observations of PAM_4-K800 carbon material. (a, b) SEM images; (c) TEM image; and (d) HR-TEM image.

and Figure S8: TEM and HR-TEM images of PAM_4-K900,).

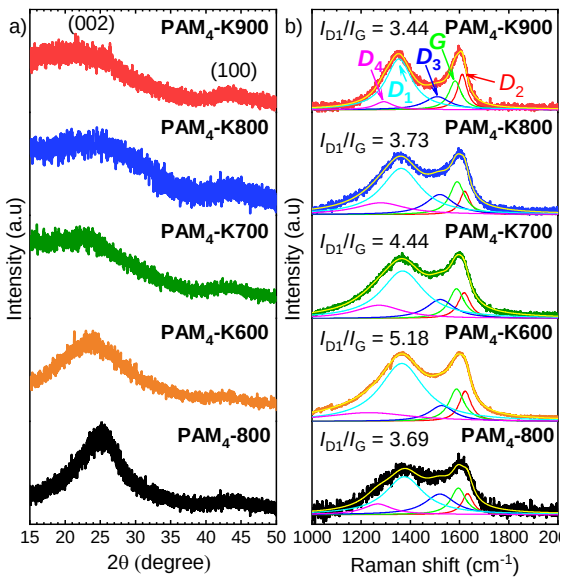

Figure 4. (a) XRD patterns and (b) Deconvoluted Raman spectra of PAM_4-800, PAM_4-K600, PAM_4-K700, PAM_4-K800, PAM_4-K900 samples.

To support the SEM observations, XRD analysis was performed. X-ray diffraction patterns of PAM_4-800, PAM_4-K600, PAM_4-K700, PAM_4-K800, and PAM_4-K900 samples are shown in Figure 4a. Two broad diffraction peaks located at around 2θ = ~24° and ~43.5° are related to the disordered structure of the amorphous carbon from (002) and (100) planes, respectively.[53] Activation with K_2CO_3 promotes abundant pores and defect site formation in the carbon lattice, which is further confirmed by the highly attenuated (002) peak. These carbon materials have many defects in their amorphous structure, low crystallinity, and good electric conductivity, which is important for supercapacitor applications. Raman spectroscopy measurements were performed to gain more information about the structural defects of the carbon materials.[54] Raman spectra show two bands located at around ~1350 and ~1600 cm^{-1}, which were deconvoluted using five Lorentzian line shapes for the D_1 (~1360 cm^{-1}), D_2 (~1620 cm^{-1}), D_3 (~1520 cm^{-1}), D_4 (~1270 cm^{-1}), and G (~1590 cm^{-1}) bands (Figure 4b).[36,55] The G band corresponds to the graphite-type lattice vibrations. D_1 band is assigned to graphene layer edges, the D_2 band is due to vibrations at the surfaces of graphitic layers, the D_3 band is characteristic of amorphous carbon and N,O-doped carbon, and the D_4 band vibration is related to polyenes and ionic impurities, for example, potassium from potassium carbonate. The ratio of peak intensities of G and D bands (I_{D1}/I_G) is called the degree of graphitization (e.g., crystallinity) and can be used to evaluate the presence of defects in the carbon structure. While carbonation temperature increases I_{D1}/I_G ratio decreases suggesting the decrease of significant structural defects or enhancement in the degree of graphitization (Figure 4b).

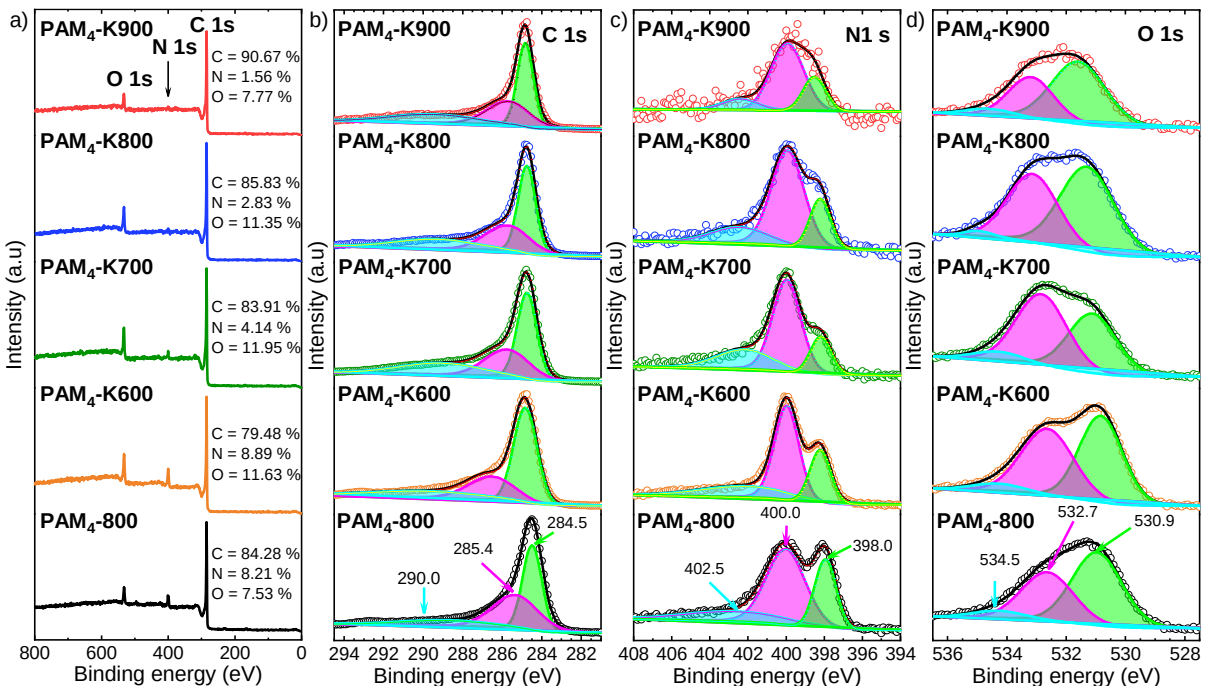

Figure 5. XPS spectra of PAM-hydrogel-derived carbons. (a) XPS survey spectra of PAM_4-800, PAM_4-K600, PAM_4-K700, PAM_4-K800, PAM_4-K900; (b) XPS C 1s core level spectra with the deconvoluted peaks; (c) XPS N 1s core level spectra with the deconvoluted peaks; (d) XPS O 1s core level spectra with the deconvoluted peaks.

The XPS technique was applied to study surface composition and functional groups present in the PAM-hydrogel-derived carbon materials (Figure 5). The survey XPS spectra show C 1s, N 1s, and O 1s components with peaks at about ~284, 400, and 532 eV, respectively (Figure 5a). The intensity of nitrogen and oxygen peaks in XPS survey spectra decreases with increasing carbonization temperature from 600 to 900 °C (Figure 5a), indicating lower contents of hydrophilic N and O functionalities in the carbon framework. Deconvolution of the C 1s spectra reveals three peaks with centers at ~284.5, 285.4, and 290.0 eV attributed to C=C (sp^2), C–C/C–N (sp^3), and O-C=O bonding states, respectively (Figure 5b). Deconvolution of N 1s spectra indicates the presence of three types of nitrogen at the surfaces of the samples (Figure 5c). The signal at ~398.0 eV belongs to the pyridinic nitrogen (N-6), that at ~400.0 eV is attributed to the pyrrolic nitrogen (N-5), and the peak at ~402.5 eV is assigned to N-oxide (N-X).[56] O 1s spectra deconvolution reveals the presence of three peaks at around ~530.9 eV, 532.7 eV, and 534.5 eV, which are attributed to carbonyl (C=O), ester (C–O–C), and carboxylic (O–C=O) groups, respectively, with C=O and C–O–C groups being the most abundant (Figure 5d). Carbonyl and ester groups enrich electrode capacitance through reversible redox reactions, whereas carboxylic groups promote charge transfer resistance, decreasing the electrode's electrochemical performance.[57] The presence of nitrogen and oxygen functionalities is favorable for fast electron transfer, but also improves the wettability of the hydrophobic carbon nanoarchitecture promoting redox reactions, which effectively contributes to the energy storage capacity.

Since the textural properties, morphology, and surface composition of these carbon materials are favorable, we decided to study their electrochemical supercapacitance properties by using CV, GCD, and EIS measurements for the three-electrode setup in an aqueous electrolyte (1M H_2SO_4). CV curves of PAM_4-800, PAM_4-K700, PAM_4-K800, and PAM_4-K900 samples at a scan rate of 5 mV s^{-1} and a potential window of -0.1−1V are shown in Figure 6a. The voltammograms have quasi-rectangular shapes, which is characteristic of an EDLC energy storage mechanism. Weak oxidation and reduction peaks at ~0.5 V and ~0.4 V, respectively, confirm the presence of nitrogen and oxygen functionalities in the carbon structure. Voltammograms for the PAM_4-K800 sample at sweep-rates of 5, 10, 20, and 40 mV s^{-1} have quasi-rectangular shape, and at higher potential sweep 60, 80, 100 mV s^{-1}, a deviation from the quasi-rectangular shape and abatement of redox peaks is observed. This behavior could be related to limitations caused by the diffusion

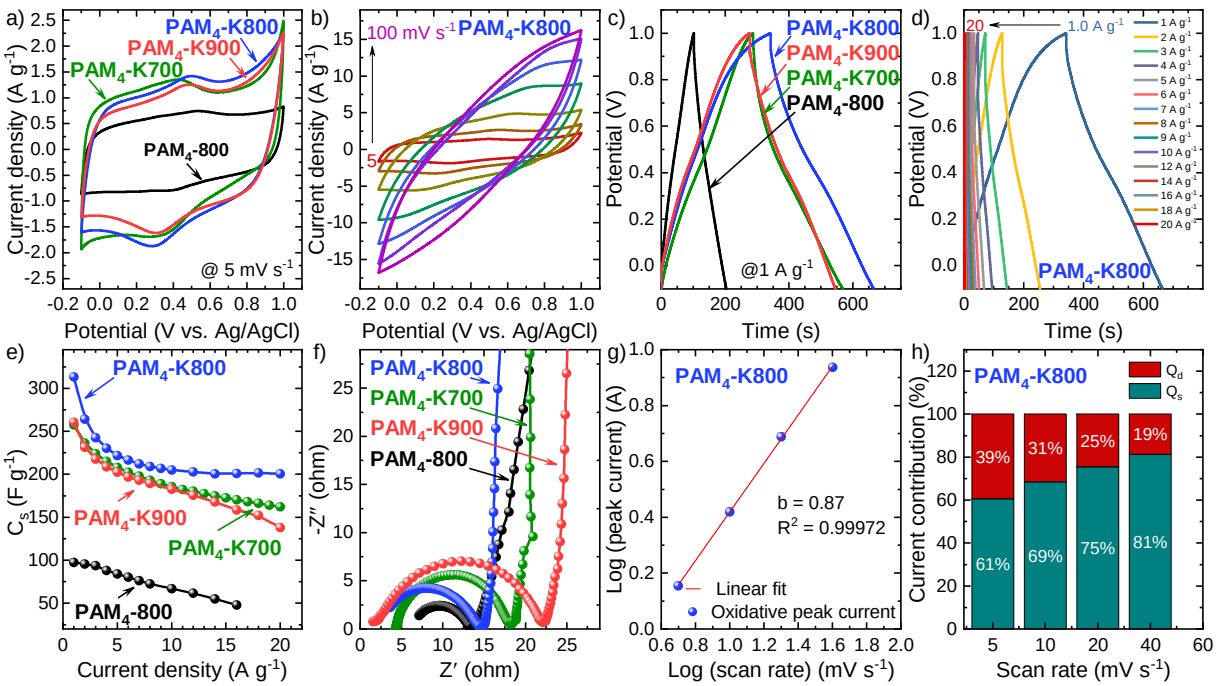

Figure 6. (a) Comparison of the CV profiles of PAM carbon-derived materials at 5 mV s^{-1}; (b) CV profile of PAM_4-K800 at different scan rates (5−100 mV s^{-1}); (c) GCD profiles of PAM_4-800, PAM_4-K700, PAM_4-K800, PAM_4-K900 measured at current density of 1 A g^{-1}; (d) GCD profiles at different current densities (1 to 20 A g^{-1}) for PAM_4-K800; (e) calculated specific capacitance C_s vs. current density; (f) Nyquist plots for PAM_4-800, PAM_4-K700, PAM_4-K800, PAM_4-K900; (g) logarithm relationship of oxidation peak current versus scan rate; (h) Capacitive or Surface-controlled (Q_s) and diffusion-controlled (Q_d) current contribution of the PAM_4-K800 electrode analyzed at various scan rates.

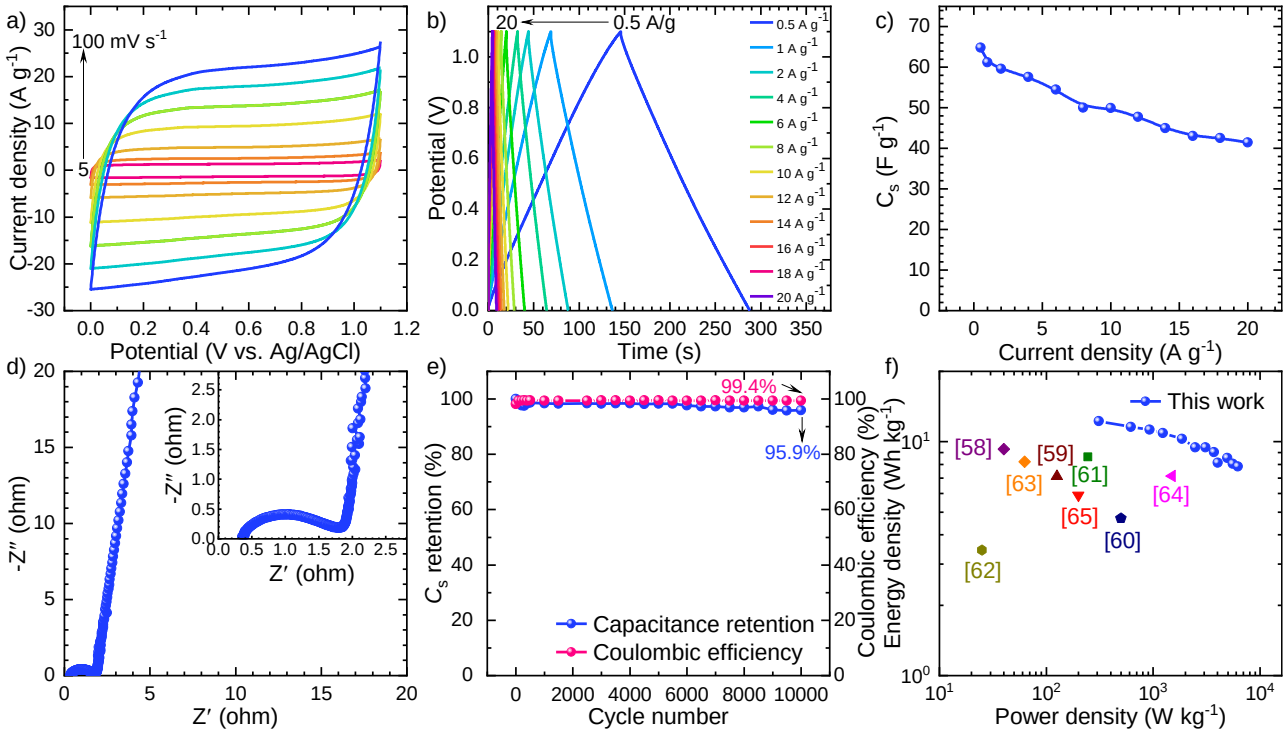

Figure 7. (a) CV profiles of PAM$_4$-K800 supercapacitor device at different scan rates (5−100 mV s^{-1}); (b) GCD curves at different current densities (0.5 to 20 A g^{-1}) in the voltage window of 0−1.1 V; (c) calculated specific capacitance C_s vs. current density; (d) Nyquist plot for the device; (e) Cycle life and Coulombic efficiency at a current density of10 A g^{-1}; (f) Ragone plot with energy density comparison with the literature.

process at the higher scan rates (Figure 6b). The GCD profiles of PAM$_4$-800 and K_2CO_3-activated PAM-hydrogel-derived carbons at the current density of 1 A g^{-1} within the potential window of -0.1 to 1.0 V are represented in Figure 6c. The GCD curves exhibit a quasi-triangular shape, thus indicating that ion storage occurs due to an EDLC mechanism. The GCD profile of the PAM$_4$-K800 sample exhibits the longest discharge time, which coincides that sample having the largest BET surface area. With increase of the current density from 1 to 20 A g^{-1} the shape of GCD curves remains quasi-triangular, manifesting efficient electrolyte ion transfer to the surface of the PAM$_4$-K800 electrode (Figure 6d, Figure S9). Data obtained from GCD measurements were used to calculate the specific capacitance C_s values applying Equation 4 and are shown in Figure 6e. PAM$_4$-K800 has the highest specific capacitance value of ~313.3 F g^{-1} at a current density of 1 A g^{-1} with a capacitance retention of ~64% at a high current density of 20 A g^{-1} (Figure S10). The obtained value of the specific capacitance is higher than the values of several other porous carbon materials derived from various carbon sources (Table S1). The data shows that 97.5% of the capacitance retention measured at 15 A g^{-1} for the PAM$_4$-K800 system is retained after 10000 cycles (Figure S11). Specific capacitances at a current density of 1 A g^{-1} for the other materials are as follows: ~257.6 F g^{-1} (PAM$_4$-K700), ~260.4 F g^{-1} (PAM$_4$-K900), ~97.3 F g^{-1} (PAM$_4$-800). Electrochemical kinetics characterization was then performed for PAM$_4$-K700, PAM$_4$-K800, PAM$_4$-K900, and PAM$_4$-800 materials using electrochemical impedance spectroscopy (Figure 6f). The Nyquist plots obtained consist of a semicircle in the high-frequency region and a vertical line in the low-frequency region for all samples. The values of the equivalent series resistance (ESR), the first intersection point on the real axis, for synthesized carbons, are as follows: 4.20 Ω (PAM$_4$-K700), 3.60 Ω (PAM$_4$-K800), 1.52 Ω (PAM$_4$-K900), 7.13 Ω (PAM$_4$-800) indicating favorable electrical conductivity. Additionally, the charge storage mechanism for the PAM$_4$-K800 sample was calculated in terms of capacitance contributions from the electrical double layer and the pseudocapacitance. As a result, the diffusion-controlled (Q_d) and surface-controlled (Q_s) or capacitive component current components were evaluated. The value of b was evaluated using Equation 5 and is 0.87 (Figure 6g), referring to the predominance of the surface-controlled or capacitive component over the diffusion-controlled mechanism, which increases with increasing scan rate (Equation 6, Figure 6h). According to the electrochemical measurements, K_2CO_3-activated PAM hydrogel-derived carbons, especially PAM$_4$-K800, show high specific capacitance values, excellent capacitance retention at high current density, and long cycle lives, rendering the materials as promising supercapacitor electrodes.

A symmetric cell device was constructed using PAM$_4$-K800 material. Its CV performance was tested in the potential window of 1.1 V at different scan rates from

5 to 100 mV s^{-1} (Figure 7a). CV profiles have a quasi-rectangular shape at low and high scan rates indicating typical electrical double-layer capacitor behavior. Figure 7b shows the charge-discharge curves of the supercapacitor device measured at various current densities (0.5 – 20 A g^{-1}). GCD profiles are essentially triangular supporting an EDLC supercapacitor energy storage mechanism. GCD data were used to calculate the gravimetric specific capacitance, which is highest at 64.8 F g^{-1} at 0.5 A g^{-1}(Figure 7c). EIS measurement was performed on the device cell prior to stability measurements in order to study the ions diffusion process at the electrode-electrolyte interface (Figure 7d). The Nyquist plot contains a semicircle in the high-frequency region and Warburg impedance in the low-frequency region. The value of ESR is ~0.36 Ω and a vertical line in the low-frequency region indicates dominant capacitive behavior with rapid diffusion of electrolyte ions. The supercapacitor cell was tested for its long-term cycling stability at a current density of 10 A g^{-1} during 10000 cycles (Figure 7e). The cell demonstrated outstanding cycle life (95.9%) and coulombic efficiency (99.4%), indicating that the excellent electrochemical stability of the electrode material is maintained. The energy and power densities of the assembled supercapacitor device were calculated and are represented in the Ragone plot (Figure 7f). The device exhibited an energy density as high as 12.3 Wh kg^{-1} at a power density of 309.4 W kg^{-1} at a current density of 0.5 A g^{-1}. The energy performance of the device is comparable or better to earlier published literature on porous carbon and other composite materials, including walnut shell-derived carbon on silver nanowires,[58] date seeds-derived carbon,[59] tamarind seeds-derived carbon,[60] hemp stem-derived carbon,[61] corn stalk-derived porous carbon,[62] spiral algae and bamboo-derived carbon,[63] graphene sheets (GNSs)–cotton cloth (CC) composite fabric,[64] PANI/N-CNT@CNT Fiber.[65] The K_2CO_3-activated PAM hydrogel-derived hierarchically porous carbons have ultra-high surface areas and are heteroatom self-doped. As a result of their textural properties, these materials are suitable candidates for supercapacitor applications with acceptable energy and power density values, and excellent cycling stability.

4. Conclusion

To summarize, we have synthesized highly porous carbon materials by carbonization (600 – 900 °C) of K_2CO_3-activated polyacrylamide (PAM) hydrogels. Modulation of the critical parameter of porosity in the carbon materials was accomplished by including an activating agent and by variation of carbonization temperature. The materials were analyzed using various techniques, namely TGA, FTIR, RAMAN, XRD, XPS, BET, SEM, and TEM. Surface compositions confirmed the presence of nitrogen and oxygen dopants in the carbon framework, which promote the capacitance of electrode materials. The most important samples were subjected to electrochemical testing using GCD, CV, and EIS measurements. The optimum sample was obtained by K_2CO_3 activation with carbonization at 800 °C, having an ultrahigh BET surface area of 3038.4 m^2 g^{-1}. In a three-electrode system, this sample showed excellent specific capacitance of 313.3 F g^{-1} at a current density of 1 A g^{-1} in an aqueous electrolyte (1M H_2SO_4) with capacitance retention after 10000 cycles being 97.5%. Furthermore, a symmetric supercapacitor device prepared using the optimum material delivered a high energy density of 12.3 Wh kg^{-1} at a power density of 309.4 W kg^{-1} demonstrating that polyacrylamide hydrogel-derived hierarchically porous carbon materials are very promising candidates as electrode materials for supercapacitor applications.

Supplementary data

Supplementary material is available at the *Bulletin of the Chemical Society of Japan*.

Funding

This work was supported by the Japan Society for the Promotion of Science (JSPS) for a JSPS postdoctoral fellowship (P21764) supported by JSPS KAKENHI Grant Number JP22KF0385. The authors are also grateful to JST-ERATO Yamauchi Materials Space-Tectonics Project (JPMJER2003) and the Queensland Node of the Australian National Fabrication Facility (ANFF-Q).

Conflict of interest statement. None declared.

References

(1) X. He, X. Zhang, *J. Energy Storage* **2022**, *56*, 106023. https://doi.org/10.1016/j.est.2022.106023.

(2) Y. Shao, M. F. El-Kady, J. Sun, Y. Li, Q. Zhang, M. Zhu, H. Wang, B. Dunn, R. B. Kaner, *Chem. Rev.* **2018**, *118*, 9233–9280. https://doi.org/10.1021/acs.chemrev.8b00252.

(3) F. Wang, X. Wu, X. Yuan, Z. Liu, Y. Zhang, L. Fu, Y. Zhu, Q. Zhou, Y. Wu, W. Huang, *Chem. Soc. Rev.* **2017**, *46*, 6816–6854. https://doi.org/10.1039/C7CS00205J.

(4) N. Wu, X. Bai, D. Pan, B. Dong, R. Wei, N. Naik, R. R. Patil, Z. Guo, *Adv. Mater. Interfaces* **2021**, *8*, 1–17. https://doi.org/10.1002/admi.202001710.

(5) H. Shao, Y.-C. Wu, Z. Lin, P.-L. Taberna, P. Simon, *Chem. Soc. Rev.* **2020**, *49*, 3005–3039. https://doi.org/10.1039/D0CS00059K.

(6) S. Najib, E. Erdem, *Nanoscale Adv.* **2019**, *1*, 2817–2827. https://doi.org/10.1039/C9NA00345B.

(7) R. G. Shrestha, S. Maji, L. K. Shrestha, K. Ariga, *Nanomaterials* **2020**, *10*, 1–27. https://doi.org/10.3390/nano10040639.

(8) J. Zhang, M. Gu, X. Chen, *Micro Nano Eng.* **2023**, *21*, 100229. https://doi.org/10.1016/j.mne.2023.100229.

(9) J. Libich, J. Máca, J. Vondrák, O. Čech, M. Sedlaříková, *J. Energy Storage* **2018**, *17*, 224–227. https://doi.org/10.1016/j.est.2018.03.012.

(10) J. Zhao, A. Burke, *J. Energy Chem.* **2020**, *59*, 276-291. https://doi.org/10.1016/j.jechem.2020.11.013.

(11) W. Ao, J. Fu, X. Mao, Q. Kang, C. Ran, Y. Liu, H. Zhang,

Z. Gao, J. Li, G. Liu, J. Dai, *Renew. Sustain. Energy Rev.* **2018**, *92*, 958–979. https://doi.org/10.1016/j.rser.2018.04.051.

(12) T. Tsubota, M. Morita, S. Kamimura, T. Ohno, *J. Porous Mater.* **2016**, *23*, 349–355. https://doi.org/10.1007/s10934-015-0087-6.

(13) F. Ma, S. Ding, H. Ren, Y. Liu, *RSC Adv.* **2019**, *9*, 2474–2483. https://doi.org/10.1039/C8RA09685F.

(14) P. Forouzandeh, V. Kumaravel, S. C. Pillai, Electrode Materials for Supercapacitors: A Review of Recent Advances. *Catalysts* **2020**, *10*, 969. https://doi.org/10.3390/catal10090969.

(15) J. Sun, W. Li, L. E, Z. Xu, C. Ma, Z. Wu, S. Liu, *J. Power Sources* **2019**, *438*, 227030. https://doi.org/10.1016/j.jpowsour.2019.227030.

(16) Z.-S. Wu, A. Winter, L. Chen, Y. Sun, A. Turchanin, X. Feng, K. Müllen, *Adv. Mater.* **2012**, *24*, 5130–5135. https://doi.org/10.1002/adma.201201948.

(17) P. Hao, Z. Zhao, J. Tian, H. Li, Y. Sang, G. Yu, H. Cai, H. Liu, C. P. Wong, A. Umar, *Nanoscale* **2014**, *6*, 12120–12129. https://doi.org/10.1039/C4NR03574G.

(18) R. R. Salunkhe, Y.-H. Lee, K.-H. Chang, J.-M. Li, P. Simon, J. Tang, L. N. Torad, C.-C. Hu, Y. Yamauchi, *Chem. Eur. J.* **2014**, *20*, 13838–13852. https://doi.org/10.1002/chem.201403649.

(19) J. Chen, J. Xu, S. Zhou, N. Zhao, C.-P. Wong, *Nano Energy* **2016**, *25*, 193–202. https://doi.org/10.1016/j.nanoen.2016.04.037.

(20) Y. Wang, Y. Liu, D. Wang, C. Wang, L. Guo, T. Yi, *Appl. Surf. Sci.* **2020**, *506*, 145014. https://doi.org/10.1016/j.apsusc.2019.145014.

(21) M. Alhabeb, M. Beidaghi, K. L. Van Aken, B. Dyatkin, Y. Gogotsi, *Carbon* **2017**, *118*, 642–649. https://doi.org/10.1016/j.carbon.2017.03.094.

(22) B. Dyatkin, O. Gogotsi, B. Malinovskiy, Y. Zozulya, P. Simon, Y. Gogotsi, *J. Power Sources* **2016**, *306*, 32–41. https://doi.org/10.1016/j.jpowsour.2015.11.099.

(23) Q.-L. Chen, K.-H. Xue, W. Shen, F.-F. Tao, S.-Y. Yin, W. Xu, *Electrochim. Acta* **2004**, *49*, 4157–4161. https://doi.org/10.1016/j.electacta.2004.04.010.

(24) G.-M. Weng, J. Li, M. Alhabeb, C. Karpovich, H. Wang, J. Lipton, K. Maleski, J. Kong, E. Shaulsky, M. Elimelech, Y. Gogotsi, A. D. Taylor, *Adv. Funct. Mater.* **2018**, *28*, 1803360. https://doi.org/10.1002/adfm.201803360.

(25) Z. Gao, Y. Zhang, N. Song, X. Li, *Mater. Res. Lett.* **2017**, *5*, 69–88. https://doi.org/10.1080/21663831.2016.1250834.

(26) H. Zhang, Y. Zhang, L. Bai, Y. Zhang, L. Sun, *J. Mater. Chem. A* **2021**, *9*, 12521–12552. https://doi.org/10.1039/D1TA00790D.

(27) A. M. Abioye, F. N. Ani, *Renew. Sustain. Energy Rev.* **2015**, *52*, 1282–1293. https://doi.org/10.1016/j.rser.2015.07.129.

(28) C. L. Gnawali, L. K. Shrestha, J. P. Hill, R. Ma, K. Ariga, M. P. Adhikari, R. Rajbhandari, B. P. Pokharel, *C Journal of Carbon Research* **2023**, *9*, 109. https://doi.org/10.3390/c9040109.

(29) R. L. Shrestha, R. Chaudhary, T. Shrestha, B. M. Tamrakar, R. G. Shrestha, S. Maji, J. P. Hill, K. Ariga, L. K. Shrestha, *Materials* **2020**, *13*, 5434. https://doi.org/10.3390/ma13235434.

(30) G.-G. Song, J. Yang, K.-X. Liu, Z. Qin, X.-C. Zheng, *Diam. Relat. Mater.* **2021**, *111*, 108162. https://doi.org/10.1016/j.diamond.2020.108162.

(31) D. R. Lobato-Peralta, A. Ayala-Cortés, A. Longoria, D. E. Pacheco-Catalán, P. U. Okoye, H. I. Villafán-Vidales, C. A. Arancibia-Bulnes, A. K. Cuentas-Gallegos, *J. Energy Storage* **2022**, *52*, 104888. https://doi.org/10.1016/j.est.2022.104888.

(32) M.-J. Kim, S. W. Choi, H. Kim, S. Mun, K. B. Lee, *Chem. Eng. J.* **2020**, *397*, 125404. https://doi.org/10.1016/j.cej.2020.125404.

(33) S. Maji, R. Chaudhary, R. G. Shrestha, R. L. Shrestha, B. Demir, D. J. Searles, J. P. Hill, Y. Yamauchi, K. Ariga, L. K. Shrestha, *ACS Appl. Energy Mater.* **2021**, *4*, 12257–12266. https://doi.org/10.1021/acsaem.1c02051.

(34) L. K. Shrestha, R. G. Shrestha, R. Chaudhary, R. R. Pradhananga, B. M. Tamrakar, T. Shrestha, S. Maji, R. L. Shrestha, K. Ariga, *Nanomaterials* **2021**, *11*, 1–16. https://doi.org/10.3390/nano11123175.

(35) M. Kim, H. Lim, X. Xu, M. S. A. Hossain, J. Na, N. N. Awaludin, J. Shah, L. K. Shrestha, K. Ariga, A. K. Nanjundan, D. J. Martin, J. G. Shapter, Y. Yamauchi, *Microporous Mesoporous Mater.* **2021**, *312*, 110757. https://doi.org/10.1016/j.micromeso.2020.110757.

(36) Y.-Q. Zhao, M. Lu, P.-Y. Tao, Y.-J. Zhang, X.-T. Gong, Z. G.-Q. Yang, Li, H. Zhang, *J. Power Sources* **2016**, *307*, 391–400. https://doi.org/10.1016/j.jpowsour.2016.01.020.

(37) H. A. Hamouda, H. I. Abdu, Q. Hu, M. A. Abubaker, H. Lei, S. Cui, A. I. Alduma, H. Peng, G. Ma, Z. Lei, *Front. Chem.* **2022**, *10*, 1–14. https://doi.org/10.3389/fchem.2022.1024047.

(38) Y. Guo, J. Bae, Z. Fang, P. Li, F. Zhao, G.Yu, *Chem. Rev.* **2020,** *120*, 7642-7707. https://doi.org/10.1021/acs.chemrev.0c00345.

(39) X. Meng, J. Zhang, Q. Chen, L. Hou, C. Yuan, *New J. Chem.* **2020**, *44*, 21279–21287. https://doi.org/10.1039/D0NJ04942E.

(40) A. Pourjavadi, H. Abdolmaleki, M. Doroudian, S. H. Hosseini, *J. Alloys Compd.* **2020**, *827*, 154116. https://doi.org/10.1016/j.jallcom.2020.154116.

(41) Q. Du, Y. Zhao, K. Zhuo, Y. Chen, L. Yang, C. Wang, J. Wang, *Nanoscale* **2021**, *13*, 13285–13293. https://doi.org/10.1039/D1NR01848E.

(42) Y. Wang, B. Ding, D. Guo, X. Wu, A *Microporous Mesoporous Mater.* **2019**, *282*, 114–120. https://doi.org/10.1016/j.micromeso.2019.03.031.

(43) Y. Yang, D. Chen, W. Han, Y. Cheng, B. Sun, C. Hou, G. Zhao, D. Liu, G. Chen, J. Han, X. Zhang, *Carbon* **2023**, *205*, 1–9. https://doi.org/10.1016/j.carbon.2023.01.013.

(44) F. Zhang, H. Liu, Z. Wu, J. Zhang, E. Cui, L. Yue, G. Hou, *ACS Appl. Energy Mater.* **2021**, *4*, 6719–6729. https://doi.org/10.1021/acsaem.1c00777.

(45) L. Miao, X. Qian, D. Zhu, T. Chen, G. Ping, Y. Lv, W. Xiong, Y. Liu, L. Gan, M. Liu, *Chinese Chem. Lett.* **2019**, *30*, 1445–1449. https://doi.org/10.1016/j.cclet.2019.03.010.

(46) H. Gao, D. Zhang, H. Zhou, J. Wu, G. Xu, Z. Huang, M. Liu, J. Yang, D. Chen, *Appl. Surf. Sci.* **2020**, *534*, 147613. https://doi.org/10.1016/j.apsusc.2020.147613.

(47) C. Fan, Y. Tian, S. Bai, C. Zhang, X. Wu, *J. Energy Storage* **2021**, *44*, 103492. https://doi.org/10.1016/j.est.2021.103492.

(48) N. Velychkivska, A. Golunova, A. Panda, P. A. Shinde, R. Ma, K. Ariga, Y. Yamauchi, J. P. Hill, J. Labuta, L. K. Shrestha, *ACS Appl. Energy Mater.* **2024**, *7*, 2906–2917. https://doi.org/10.1021/acsaem.4c00141.

(49) X. Zhang, M. Han, A. Fuseni, A. M. Alsofi, *J. Pet. Sci. Eng.* **2019**, *180*, 518–525.

https://doi.org/10.1016/j.petrol.2019.04.092.
(50) L. H. Gaabour, *Results Phys.* **2017**, *7*, 2153–2158. https://doi.org/10.1016/j.rinp.2017.06.027.
(51) A. M. Dumitrescu, G. Lisa, A. R. Iordan, F. Tudorache, I. Petrila, A. I. Borhan, M. N. Palamaru, C. Mihailescu, L. Leontie, C. Munteanu, *Mater. Chem. Phys.* **2015**, *156*, 170–179. https://doi.org/10.1016/j.matchemphys.2015.02.044.
(52) L. K. Shrestha, Z. Wei, G. Subramaniam, R. G. Shrestha, R. Singh, M. Sathish, R. Ma, J. P. Hill, J. Nakamura, K. Ariga, *Nanomaterials* **2023**, *13*, 1–17. https://doi.org/10.3390/nano13050946.
(53) Z.-W. Ma, H.-Q. Liu, Q.-F. Lü, *J. Energy Storage* **2021**, *40*, 102773. https://doi.org/10.1016/j.est.2021.102773.
(54) J. H. Khan, J. Lin, C. Young, B. M. Matsagar, K. C. W. Wu, P. L. Dhepe, M. T. Islam, M. M. Rahman, L. K. Shrestha, S. M. Alshehri, T. Ahamad, R. R. Salunkhe, N. A. Kumar, D. J. Martin, Y. Yamauchi, M. S. A. Hossain, *Mater. Chem. Phys.* **2018**, *216*, 491–495. https://doi.org/10.1016/j.matchemphys.2018.05.082.
(55) A. Sadezky, H. Muckenhuber, H. Grothe, R. Niessner, U. Pöschl, *Carbon* **2005**, *43*, 1731–1742. https://doi.org/10.1016/j.carbon.2005.02.018.
(56) A. J. R. Rennie, P. J. Hall, *Phys. Chem. Chem. Phys.* **2013**, *15*, 16774. https://doi.org/10.1039/c3cp52233d.
(57) Y.-R. Zhao, C.-C. Liu, Q.-Q. Lu, O. Ahmad, X.-J. Pan, M. Daria, *New Carbon Mater.* **2022**, *37*, 875–897. https://doi.org/10.1016/S1872-5805(22)60637-1.
(58) Q. Bai, G. Zhang, X. Bai, Y. Liu, Y. Wang, C. Li, Y. Shen, H. Uyama, *Applied Surface Science* **2024**, *678*, 161140. https://doi.org/10.1016/j.apsusc.2024.161140.
(59) R. Farma, A. Indriani, and I. Apriyan, *J Mater Sci: Mater Electron* **2023**, *34*, 81. https://doi.org/10.1007/s10854-022-09446-5.
(60) M. Raja, B. Sadhasivam, R. J. Naik, R. Dhamodharan and K. Ramanujam, *Sustainable Energy Fuels*, **2019**, *3*, 760-773. https://doi.org/10.1039/c8se00530c.
(61) D. Qiu, C. Kang, A. Gao, Z. Xie, Y. Li, M. Li, F. Wang, and R. Yang, *ACS Sustainable Chem. Eng.* **2019**, *7*, 14629−14638. https://doi.org/10.1021/acssuschemeng.9b02.
(62) Y. Zhang, Y. Cai, T. Li, M. Wang, X. Chen, and Y. Xu, *J Mater Sci: Mater Electron*, **2024** *35*, 116. https://doi.org/10.1007/s10854-024-11944-7.
(63) W. Yue, Z. Yu, X. Zhang, H. Liu, T. He, *Journal of Analytical and Applied Pyrolysis*, **2024**, *178*, 106409. https://doi.org/10.1016/j.jaap.2024.106409.
(64) W. W. Liu, X. B. Yan, J. W. Lang, C. Peng and Q. J. Xue, *J. Mater. Chem.*, **2012**, *22*, 17245-17253. https://doi.org/10.1039/C2JM32659K.
(65) J. Tian, N. Cui, P. Chen, K. Guo and X. Chen, *J. Mater. Chem. A*, **2021**, *9*, 20635–20644. https://doi.org/10.1039/D1TA03663G.